



A comparison of two quasi-static computational models for assessment of intra-myocardial injection as a therapeutic strategy for heart failure

Title	A comparison of two quasi-static computational models for assessment of intra-myocardial injection as a therapeutic strategy for heart failure
Author(s)	Fan, Yiling;Ronan, William;Teh, Irvin;Schneider, Jurgen E.;Varela, Claudia E.;Whyte, William;McHugh, Peter;Leen, Sean B.;Roche, Ellen T.
Publication Date	2019-05-06
Publisher	Wiley
Repository DOI	10.1002/cnm.3213

A comparison of two quasi-static computational models for assessment of intra-myocardial injection as a therapeutic strategy for heart failure

Yiling Fan^{1,2}, William Ronan³, Irvin Teh^{4,5}, Jurgen E. Schneider^{4,5}, Claudia E Varela^{6,7}, William Whyte⁸⁻¹², Peter McHugh³, Sean Leen¹, Ellen Roche^{2,6}

¹ Mechanical Engineering, College of Engineering and Informatics, National University of Ireland Galway, Ireland.

² Department of Mechanical Engineering, Massachusetts Institute of Technology, Cambridge, MA, USA.

³ Biomechanics Research Centre, Biomedical Engineering, College of Engineering and Informatics, National University of Ireland Galway, Ireland.

⁴ Leeds Institute of Cardiovascular and Metabolic Medicine, University of Leeds, UK.

⁵ Division of Cardiovascular Medicine, Radcliffe Department of Medicine, University of Oxford, Oxford, OX3 7BN, UK.

⁶ Institute for Medical Engineering Science, Massachusetts Institute of Technology, Cambridge, MA, USA.

⁷ Harvard-MIT Program in Health Sciences and Technology, 77 Massachusetts Avenue, Room E25-518, Cambridge, MA 02139, USA

⁸ Tissue Engineering Research Group, Department of Anatomy, Royal College of Surgeons in Ireland (RCSI), 123 St. Stephens Green, Dublin 2, Ireland

⁹ Trinity Centre for Bioengineering, Trinity College Dublin (TCD), College Green, Dublin 2, Ireland

¹⁰ Advanced Materials and BioEngineering Research (AMBER) Centre, RCSI, NUIG & TCD, Dublin 2, Ireland

¹¹ John A Paulson School of Engineering and Applied Sciences, Harvard University, 29 Oxford Street, Cambridge, MA 02138, USA

¹² Wyss Institute for Biologically Inspired Engineering, Harvard University, 60 Oxford Street, Cambridge, MA 02138, USA

Abstract and key terms

Myocardial infarction, or heart attack, is the leading cause of mortality globally. Although the treatment of myocardial infarct has improved significantly, scar tissue that persists can often lead to increased stress and adverse remodeling of surrounding tissue, and ultimately to heart failure. Intra-myocardial injection of biomaterials represents a potential treatment to attenuate remodeling, mitigate degeneration and reverse the disease process in the tissue. *In vivo* experiments on animal models have shown that this therapeutic strategy results in functional benefits. However, poor understanding of the mechanism, the optimal injection pattern, volume and material has acted as barriers to its widespread clinical adoption. In this study, we developed two quasi-static finite element simulations of the left ventricle to investigate the mechanical effect of intra-myocardial injection. The first model employed idealized left ventricle geometry with rule-based cardiomyocyte orientation. The second model employed subject-specific left ventricle geometry with cardiomyocyte orientation from diffusion tensor magnetic resonance imaging. Both models predicted cardiac parameters including ejection fraction, systolic wall thickening, and ventricular twist that matched experimentally reported values. All injection simulations showed cardiomyocyte stress attenuation, offering an explanation for the mechanical reinforcement benefit associated with injection. The study also enabled a comparison of injection location, and corresponding effect on cardiac performance at different stages of the cardiac cycle. While the idealized model has lower fidelity, it predicts cardiac function and differentiates the effects of injection location. Both models represent versatile *in silico* tools to guide optimal strategy in terms of injection number, volume, site, and material properties.

Key terms: Finite Element Method, Intra-myocardial Injection, Cardiac Modeling, Diffusion Tensor Imaging, Diffusion Tensor Magnetic Resonance Imaging.

Introduction

Coronary artery disease (CAD) is the number one cause of adult mortality worldwide resulting more than 8 million deaths in 2015 according to the World Health Organization (WHO)[1]. Myocardial infarction (MI), also known as heart attack, is a common result of CAD. After an MI, revascularization with stents or angioplasty balloons is a primary interventional treatment that has been successful in recent years. However, post-MI scar tissue in the heart can result in a cascade of adverse remodeling, ultimately leading to heart failure. Therapies, both medical[2] and mechanical[3,4], are currently employed to maintain cardiac function and reduce mortality associated with post-MI heart failure. Recently, the use of biomaterials injected directly into the heart muscle (myocardium) to prevent or attenuate adverse post-MI remodeling has become a viable therapy, and an area of growing research focus. Minimally invasive devices have been developed for delivering biomaterials through the endocardium[5] or the epicardium[6] and studies have used a range of hydrogels in pre-clinical and clinical experiments, demonstrating an ability to decrease stress in the myocardial wall by modifying the mechanical properties and increasing wall thickness. These studies indicate that the mechanical reinforcement provided by the injected biomaterial can prevent MI progression [7–10].

Although intra-myocardial injection of biomaterials has been successful in pre-clinical models, the mechanism behind these effects has not been fully elucidated. To further understand and guide this therapeutic strategy, computational models have been employed to simulate cardiac mechanics and remodeling post-injection. Largely, these simulations can be divided into static and dynamic models. Static models predict a specific stage of a cardiac cycle: end-systole (ES), the end of the contracting phase; or end-diastole (ED), the end of the relaxation phase. They are simpler and less computationally intensive than dynamic models that simulate the entire cardiac cycle.

Reported models also vary in relation to the assumptions made for mechanical properties of tissue. Cardiac tissue is generally modelled as a hyper-elastic material, with multiple constitutive models reported in the literature[11,12]. Static simulations only model the passive myocardial behavior, or the response to pressure changes, and can show the effect of intra-myocardial injection at one point in the cycle, usually at ED[12–14]. For example, the Fung model[15], a strain-based function, is a widely used constitutive model for the passive material properties of myocardium in cardiac mechanical simulations[12,14,16]. This transversely isotropic hyper-elastic model represents the anisotropic behavior of the cardiac tissue, in which the cardiomyocyte direction is much stiffer than the sheetlet direction or sheetlet-normal direction (also referred to as the cross-cardiomyocyte direction). An alternative material model is invariant-based[17] and can incorporate non-orthogonal cardiomyocyte orientation. For dynamic models, the general approach is to add a time-dependent active tension[18–20] or active strain[21–24] to the hyper-elastic constitutive model to simulate active contraction during systole.

For simplification, a truncated ellipsoid geometry is generally used to represent the geometry of the left ventricle (LV). It is usually mapped with transmurally varying helicoid cardiomyocyte orientation, where the ventricular cardiomyocytes orient in opposing helices at the endocardium (inner surface) and epicardium (outer surface), with circumferential orientation in the middle layer. This specific cardiomyocyte orientation lends itself to the twisting motion of the heart and ensures the ejection of blood upward out of the ventricle. In one of the earliest computational models of intra-myocardial injection, Wenk et al [25] developed a dynamic model that demonstrates cardiomyocyte stress reduction of the LV at both ED and ES on injection of polymeric materials into the myocardial wall. The polymeric injections were modelled as inclusions in the myocardium with isotropic material properties using the Mooney–Rivlin model. Subsequently, the injection simulation created by Kortsmits et al [26] included the microstructure of the biomaterial. A realistic representation of biomaterial distribution in the myocardium was included in their DTI-based LV geometry that successfully showed both biomechanical and functional improvements after post-MI injection.

Here, we develop two computational models of the LV: (i) an idealized model with a rule-based helicoid cardiomyocyte arrangement and (ii) a diffusion tensor magnetic resonance imaging (DT-MRI or DTI) model with actual cardiomyocyte orientation data. We use a thermal analogy to simulate active contraction, enabling implementation of anisotropic strain. In both models, we simulate (i) a healthy baseline, (ii) a myocardial infarct, and (iii) two different injection strategies, one pattern where a hydrogel material is injected directly into the infarct and the other where the material is injected into the border zone between the infarcted and healthy tissue. Within each model, we compare cardiomyocyte stress (also referred to as fiber stress) in the infarct and border zone for each injection pattern. Next, we compare the two models to each other and to reported experimental ranges of functional parameters such as ejection fraction (EF) and LV twist.

Materials and Methods

Idealized LV Model

For the idealized LV model (Fig. 1a), we used the truncated ellipsoid geometry adopted from Kichula et al.[12] with transmurally varying helical cardiomyocyte orientation, which was verified in previous cardiac DTI studies [27,28]. It was discretized with 15768 hexahedral elements (C3D8) in Abaqus (Dassault Systèmes, Providence, RI, USA)[29]. The cardiomyocyte arrangement was based on the Holzapfel & Ogden[17] model, in which cardiomyocyte angle varies from an angle of 60° at the endocardium to an angle of -60° at the epicardium relative to the basal plane. The sheetlet-normal direction (n) and the sheetlet direction (s), which were on the cross-cardiomyocyte plane, were defined to be orthogonal to the cardiomyocyte direction (Fig. 1b-d). This empirical helicoid cardiomyocyte orientation was generated on the ellipsoid LV by assigning discrete local orientations, layer by layer.

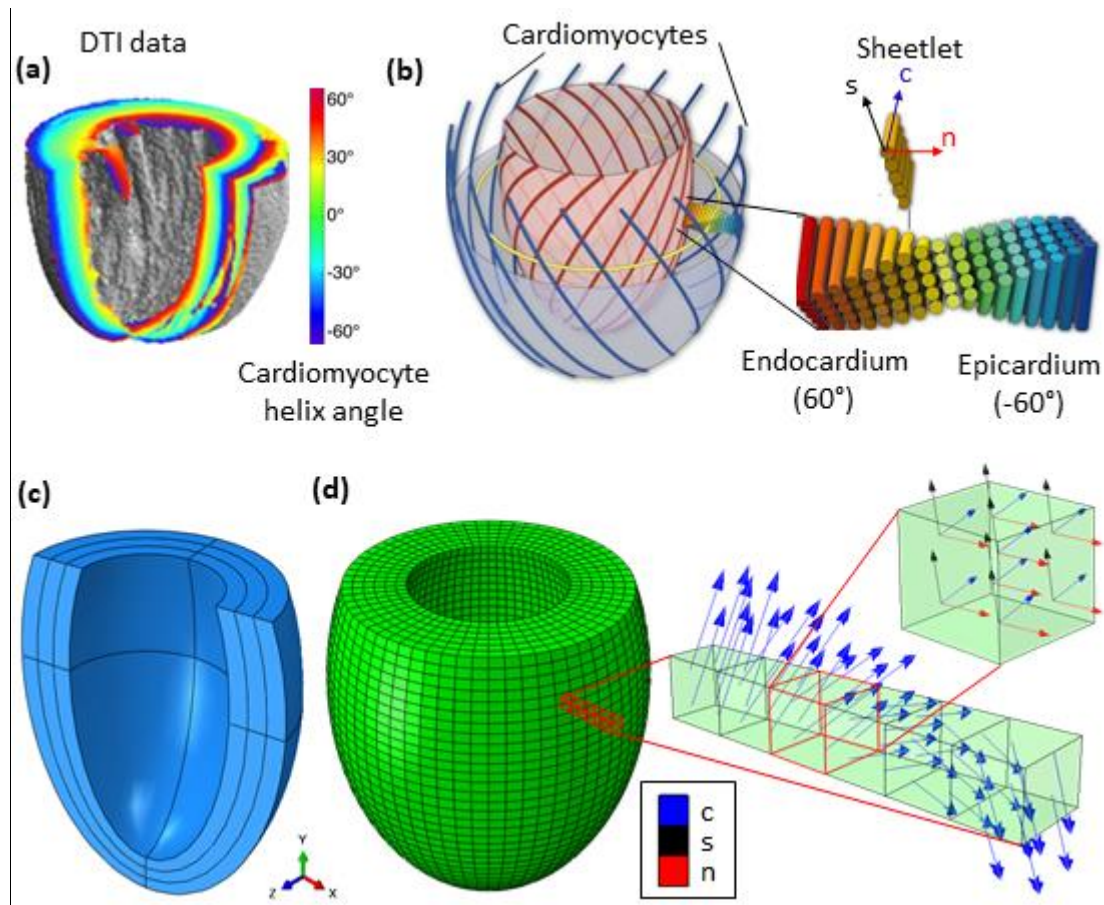


Figure 1. The idealized left ventricle model. (a) Cardiomyocyte helix angle across the ventricular wall (adapted with permission from [28]). (b) Demonstration of cardiomyocyte orientation and sheetlet orientation in the LV (adapted with permission from [27]). (c) Long-axis cut-view of the truncated ellipsoid LV model. The geometry is partitioned to 3 layers in order to create a structure mesh which can be assigned with transmurally varying local orientation. (d) rule-based cardiomyocyte orientation, with cardiomyocytes transmurally varying from -60° at the epicardium (outer surface of the ventricle) to 60° at the endocardium (inner surface of the ventricle). Angles are relative to the basal (top) plane of the ellipsoid. Cardiomyocyte (c), sheetlet (s), and sheetlet-normal (n) directions are shown in a single element.

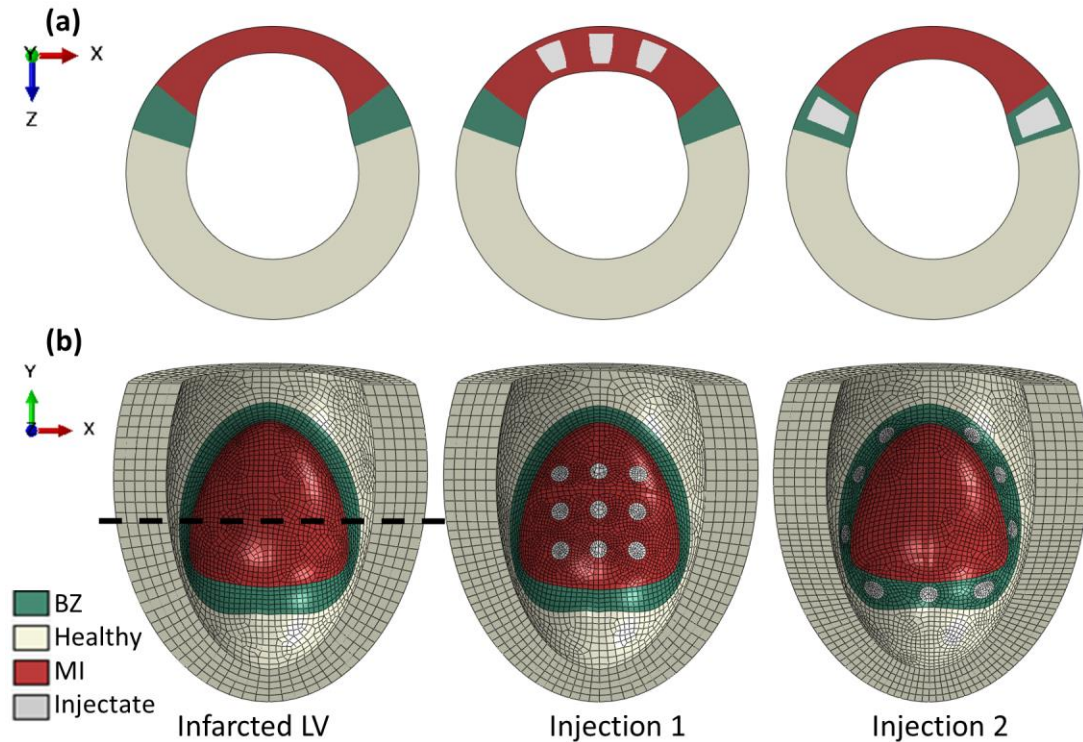


Figure 2. Idealized Model Injection Overview. Transverse plane views (a) of the LV show post-MI wall thinning and post-injection localized wall thickening. Longitudinal cross-section views (b) of LV illustrate infarct size and injection patterns. The dashed lines indicate the locations of the transverse planes. BZ=border zone, MI=myocardial infarct.

Using the idealized geometry, an MI model and two injection models were constructed by changing the material properties and geometry around the infarcted region, shown in Fig. 2a,b. All infarcts were modeled as transmural infarcts. The wall thickness was reduced by 50% in the infarcted region, similar to a 2-week infarcted heart observed by Quinn et al[30], and the wall thickness gradually increased at the border zone (BZ), which was defined as the tissue up to 2 mm away from the infarct margin. Two injection models, Idealized Injection 1 and Idealized Injection 2, were created, with 9 injections in the infarct region or BZ, respectively. The total injection volumes in both cases were approximately 4 mm³. Localized wall thickening was performed in order to compensate for the additional volume created by the injections. For Injection 1, the infarct wall thickness was increased back to 80% of the normal thickness as reported[10]. For Injection 2, it was only increased back to 60% since the injections were in the BZ. As reported in Table S3, the volume ratio of remote, border zone and infarct tissue were maintained for all simulations. The details of modifications for each diseased model are summarized in Table 1.

DTI-based LV Model

For the subject-specific model, we used an anatomically accurate rat geometry with cardiomyocyte orientation obtained from DT-MRI imaging as described in a previous study by

our co-authors[28]. The LV geometry was segmented and reconstructed using Mimics and 3-Matics Software (Materialise, Leuven Belgium) and discretized in Abaqus with 21384 C3D8 elements, shown in Fig. 3a-c. As described in the Supplementary Methods, the primary eigenvectors derived from DTI data were mapped onto the FE mesh as local element orientations. The resulting cardiomyocyte arrangement is consistent with the widely accepted helical structure of myocardial tissue[31]. The geometry modification and segmentation for the diseased models in the DTI case were the same as in the Idealized case. Infarct size and injection locations are shown in Fig. 4a,b.

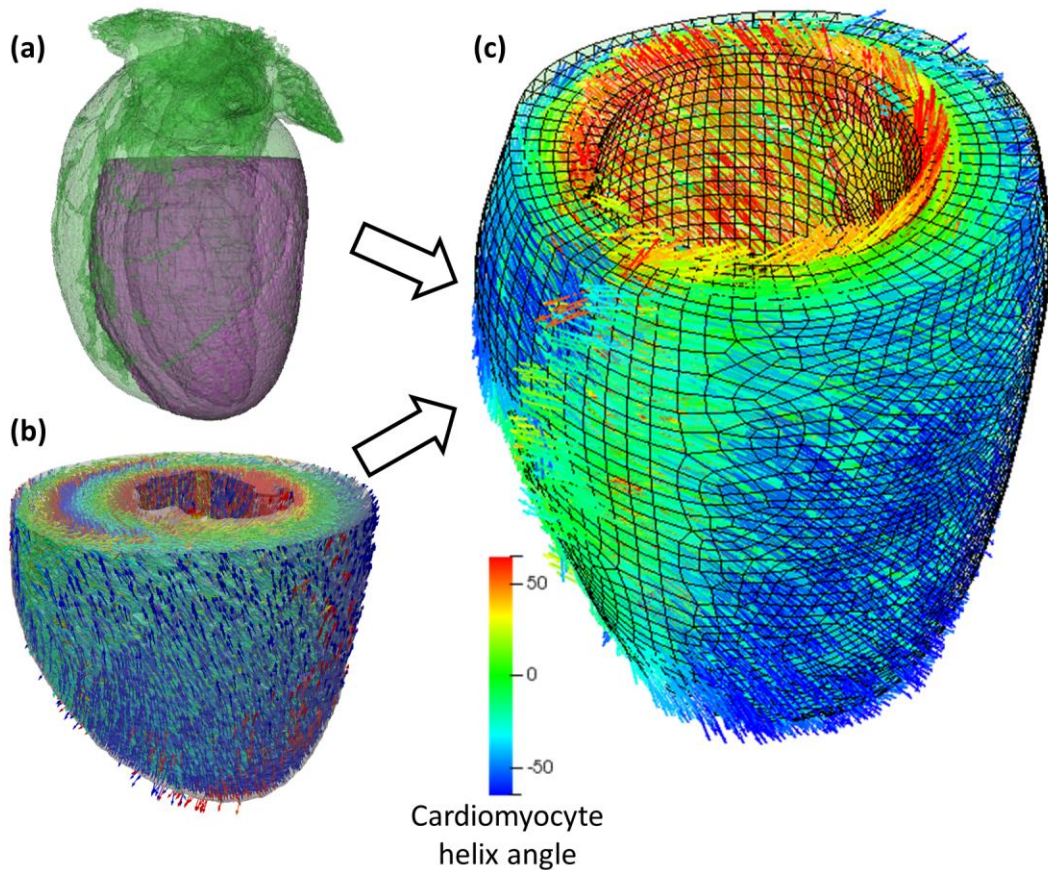


Figure 3. The DT-MRI data. (a) Reconstructed MRI of a whole rat heart (green) with LV (purple) segmented; (b) DTI data; (c) DTI data mapped on the FE model.

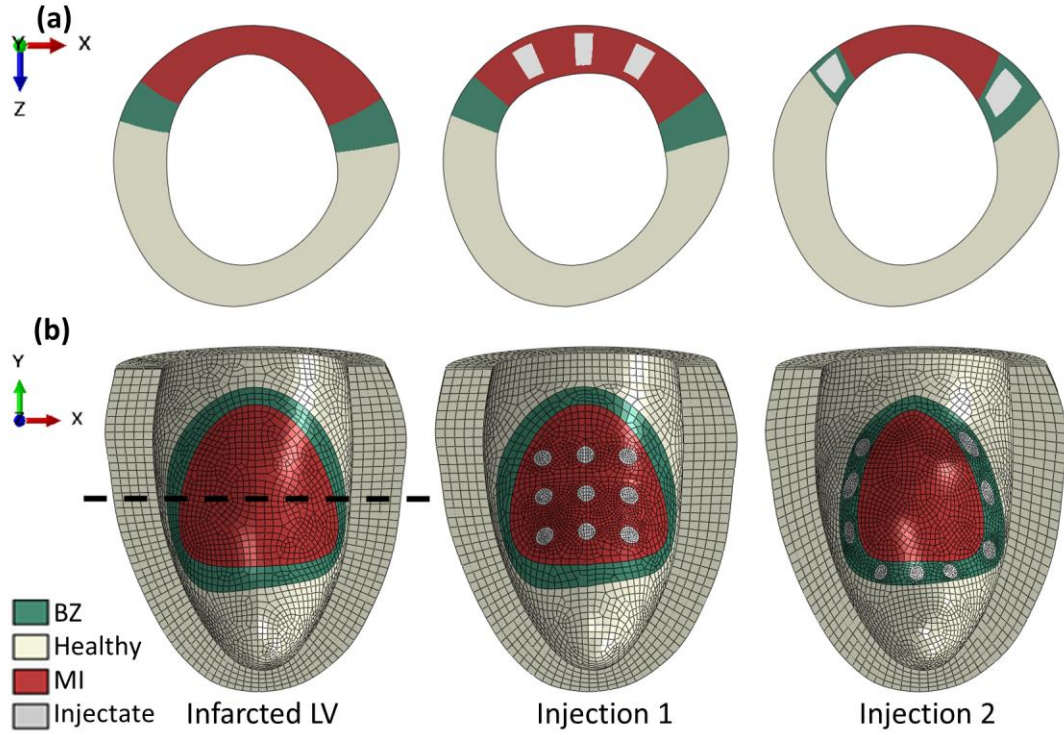


Figure 4. DTI-based Model Injection Overview. The changes of wall thickness are shown in transverse plane views (a) and the injection patterns are shown in longitudinal cross-section views (b). The dashed lines indicate the locations of the transverse planes.

Simulation Approach

The same material models, boundary conditions and simulation configuration were applied to the Idealized and DTI-based FE models. The passive behavior of the myocardium was modeled as a transversely isotropic hyper-elastic model with the Fung strain energy density function, which has the form[29]:

$$\psi(\mathbf{E}) = \frac{C_0}{2} (e^{Q(\mathbf{E})} - 1) + \frac{1}{D} \left(\frac{(J^{el})^2 - 1}{2} - \ln(J^{el}) \right) \quad (1)$$

where C_0 is an elastic constant, Q is an exponent as, which is a function of Green-Lagrange strain tensor \mathbf{E} , D is equal to $\frac{2}{K}$ (K is bulk modulus) and J^{el} is the elastic volume ratio.

Since the myocardium has low compressibility, it has a high value of bulk modulus that causes D to be close to zero. The transversely isotropic form of the exponential term proposed by Guccione et al[32] was employed as follows:

$$Q(\mathbf{E}) = b_f E_{ff}^2 + b_t (E_{ss}^2 + E_{nn}^2 + E_{sn}^2 + E_{ns}^2) + b_{ft} (E_{fs}^2 + E_{sf}^2 + E_{fn}^2 + E_{nf}^2) \quad (2)$$

where the subscript c , s , and n indicate the cardiomyocyte, sheetlet, and sheetlet-normal

directions; and b_f , b_t , and b_{ft} are the dimensionless transversely isotropic material constants associated with the strain tensor.

The coefficients for Equation (2) were replicated from Kichula et al[12], where C_0 was 0.679 kPa and b_f , b_t , and b_{ft} were 20.97, 3.346, and 12, respectively.

An active strain term, implemented via the thermal strain tensor in Abaqus, was introduced to mimic the active contraction. The thermal strain tensor can be simply expressed as:

$$\boldsymbol{\varepsilon}_{th} = \boldsymbol{\alpha}\Delta T \quad (3)$$

where $\boldsymbol{\alpha}$ is the thermal expansion coefficient tensor, and ΔT is the temperature difference, which was set to be 1 in all simulations. The thermal expansion coefficient in the cardiomyocyte direction was set to $\alpha_{ff} = -0.32$, or a contraction of 32%, which is comparable with the fractional shortening of a healthy rat heart [33]. To maintain the near-incompressibility of myocardial tissue, the expansion coefficients in the sheetlet and sheetlet-normal direction were set to $\alpha_{ss} = \alpha_{nn} = 0.21$. All other terms in $\boldsymbol{\alpha}$ are set to zero. This analogy enabled implementation of an orthotropic strain where the cardiac tissue contracted by 32% in the cardiomyocyte direction and expanded by 21% in the two orthogonal directions. The active strain method[21–24] is used to represent contractility. In order to couple the active and passive (elastic) components, the total deformation gradient (\boldsymbol{F}) is the multiplication of the elastic (\boldsymbol{F}_e) and thermal (\boldsymbol{F}_{th}) deformation gradients (Equation (4)). \boldsymbol{F}_e is used to determine the Green-Lagrange tensor \boldsymbol{E} as described in Equation (5) and \boldsymbol{E} is used in Equation (2). \boldsymbol{F}_{th} is determined from the thermal strain $\boldsymbol{\varepsilon}_{th}$, which is interpreted by Abaqus as a nominal strain.

$$\boldsymbol{F} = \boldsymbol{F}_e \boldsymbol{F}_{th} \quad (4)$$

$$\boldsymbol{E} = \frac{1}{2}(\boldsymbol{F}_e^T \boldsymbol{F}_e - \boldsymbol{I}) \quad (5)$$

The Fung model was also used for the infarct, with stiffness (C_0) increased to 50 times that of the normal myocardium, as described in Wenk et al.[16] and the contractility was removed by setting the thermal strain expansion coefficient to zero. The BZ myocardium was set to have normal passive properties with 50% less contractility since it is the transition region between healthy and infarcted tissues. The material parameters for different types of myocardium are summarized in Table S1. The injection material was assumed to be the hydroxyphenyl derivative of hyaluronic acid derivative (HA-PH-RGD) hydrogel, which was used in a study by Dolan et al [34]. Compression data was fitted with the Neo-Hookean model to give a Young's modulus of 70 kPa, slightly higher than the value used for the normal myocardium.

The simulation contained two steps, diastole and systole, with ED pressure (10 mmHg) and ES pressure (120 mmHg), respectively, being applied to the endocardial surface. These pressures represented well-established values for diastolic and systolic pressures, respectively. Dirichlet

boundary conditions are applied on the base of the LV using a cylindrical coordinate. All basal nodes are fixed in the longitudinal direction and the endocardial ring is also fixed in the angular direction. All models were run using the Abaqus/Explicit solver. Mass scaling was used to provide feasible computation times and the kinetic energy of the system was monitored to ensure that the response was quasi-static, (i.e. kinetic energy was less than 5% of the internal energy). As the incompressible constraint cannot be enforced by Abaqus in an explicit solution scheme[29], the myocardium was modelled using the so-called slightly compressible approach, which has recently been shown to be more accurate to represent the myocardium[35]. The run-time of each simulation was approximately 8 hours on a CentOS cluster with three nodes, each consisting of a Xeon E5-2650 processor.

Experimental Verification

Baseline data of LV function was collected from Sprague Dawley rats (200-225g) in accordance with the Institute for Animal Care and Use Committee, Harvard University/Brigham and Women's Hospital. Details are described in the Supplementary Materials. Intraventricular pressure-volume measurements were taken for EF (SPR-838, AD instruments) and echocardiographic data was used for systolic wall thickness measurements (Vevo 2100, Visual Sonics).

Results

The idealized and DTI-based models can both recreate reasonable physiological features of a healthy LV as shown in Figs. 5a,b. Both models predicted slightly lower EF but systolic wall thickening (SWT) predictions were within the experimental range. The idealized model showed clockwise rotation at the base and counter-clockwise rotation at the apex when viewing from the apex (Fig. 5c), consistent with clinical measurements[36]. However, the DTI-based model demonstrated clockwise rotation at both the base and the apex (Fig. 5d) which is inconsistent with clinical reports.

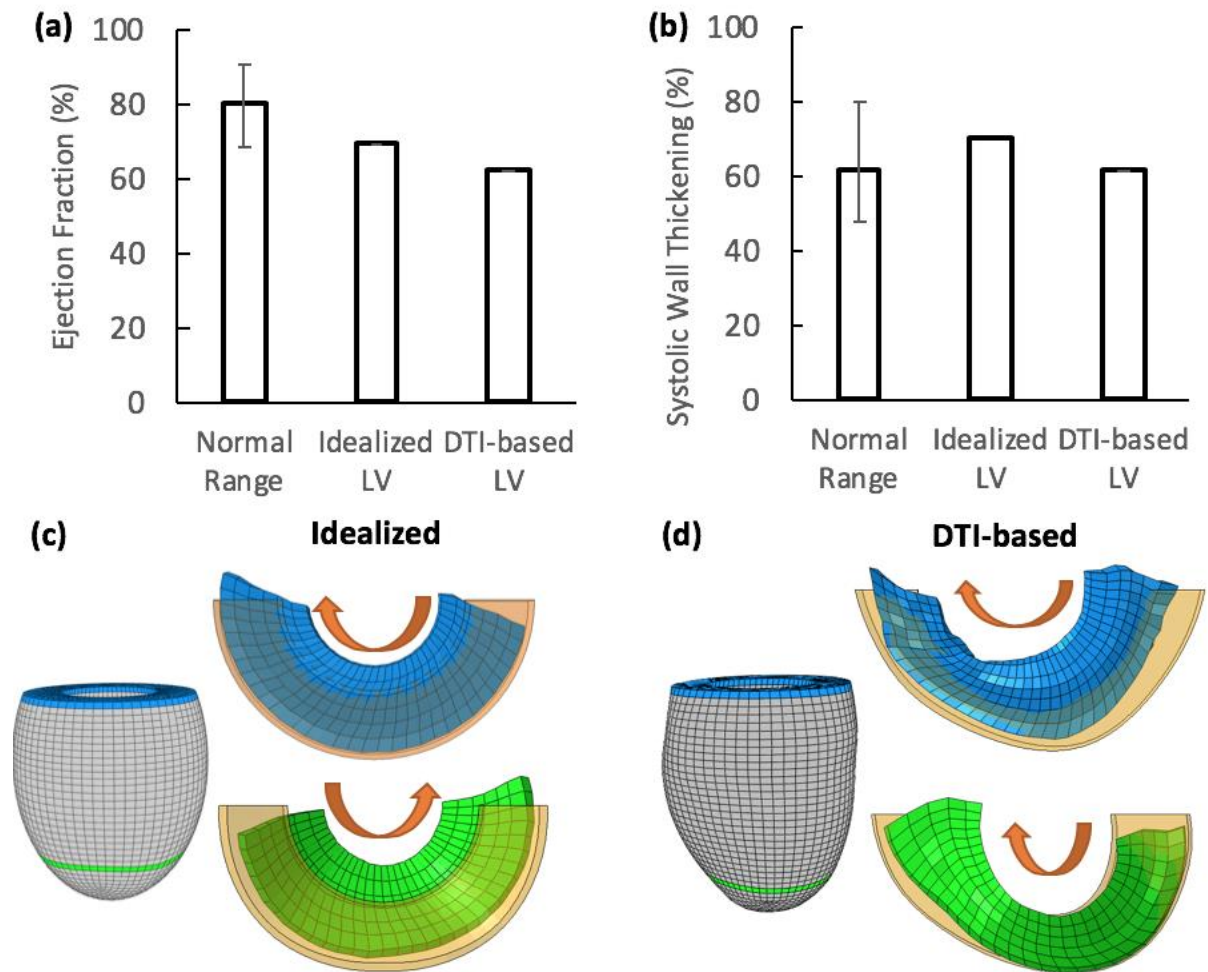


Figure 5. Comparison of cardiac functions predicted by the idealized model, DTI-based model and the published normal ranges. (a, b) The ranges of ejection fraction and systolic wall thickening were measured from rat hearts by pressure-volume catheter and ultrasound, respectively. (c, d) Basal plane (blue) and apical plane (green) twist of the idealized and DTI-based models, showing initial (transparent) and deformed (solid) respectively viewed from the apex.

Idealized Model Stresses

In the idealized case (Fig. 6), the MI induced stress around the border of the infarct at end-diastole (ED) in the range of 4 kPa to more than 8 kPa, near the endocardium. At end-systole (ES), the MI induced high stresses radiated to the BZ and the remote region especially near the epicardium. With injections in the infarct (Injection 1), the predicted ED stresses were globally reduced in both the infarct and BZ. Some high stress areas around the endocardial infarct border remained. At ES, the majority of the high endocardial stresses in the infarct were reduced with small regions of stress concentration (along the cardiomyocyte orientation) visible around the injections. Injection 1 also reduced the ES epicardial stresses around the infarct and BZ but not the remote region. Similarly, injections in the BZ (Injection 2) reduced

both the infarct and BZ stresses at both ED and ES although not as much as Injection 1 notably near the endocardium. Stress concentration was also noted around the injections.

The volume-averaged cardiomyocyte stress, an average stress normalized by the total volume of elements in a certain region, was calculated to quantify the mechanical effect of the MI and the injection treatments. At ED, the stresses in the infarct and the BZ were predicted to increase by 46.9% and 9.5%, respectively due to the MI. At ES, the stresses were increased by 40.2% and 44.5% in the corresponding regions. After Injection 1, ED stresses were predicted to reduce by 27.9% and 14.9% in the infarct and BZ, respectively. Less significant effects were predicted with Injection 2, where infarct and BZ stresses were reduced by 5.9% and 3.8% at ED, respectively. Similarly, the infarct stresses were reduced by 41.1% after Injection 1 and 7.9% after Injection 2 at ES. The BZ stresses at ES were reduced by 19.3% after Injection 1 while increased by 0.9% after Injection 2.

We defined a critical stress threshold at 8 kPa at ED and 60 kPa at ES, and show critical stresses over these thresholds in red in the contour plots. The critical stress volume (CSV), or the volume of elements above the critical stress threshold, was calculated at both ED and ES. For the MI model, the CSV was 7.6 mm³ and 7.7 mm³ at ED and ES, respectively. After Injection 1, the relative values were reduced to 6.6 mm³ and 3.6 mm³, showing the benefits of injections. After Injection 2, the CSV was also reduced to 7.4 mm³ and 5.1 mm³ at ED and ES, respectively.

As shown in the contour plots, the mechanical effects of injections were most notable in the endocardium especially in ES. The tissue in the BZ is a critical region of viable tissue that can potentially be salvaged. Therefore, we further evaluated the injection effects around the BZ, shown in Fig. 7. Fig. 7a shows the critical volume ratio which is the ratio between the CSV and the associated BZ volume in each model. After Injection 1, the volume ratio was reduced at both ED and ES while Injection 2 only reduced the ratio at ED. Volume-averaged stresses in this subregion were isolated and plotted in Fig. 7b. Both injection strategies were able to reduce the average stress but neither reduced them to baseline. The stress distribution histograms (Fig. 7c,d) showed that all three diseased models had larger high stress regions than the baseline healthy model. The number of high stress regions was slightly lower after Injection 1 but not substantially reduced with Injection 2. Additional details of the regional stress histograms are shown in Fig. S1.

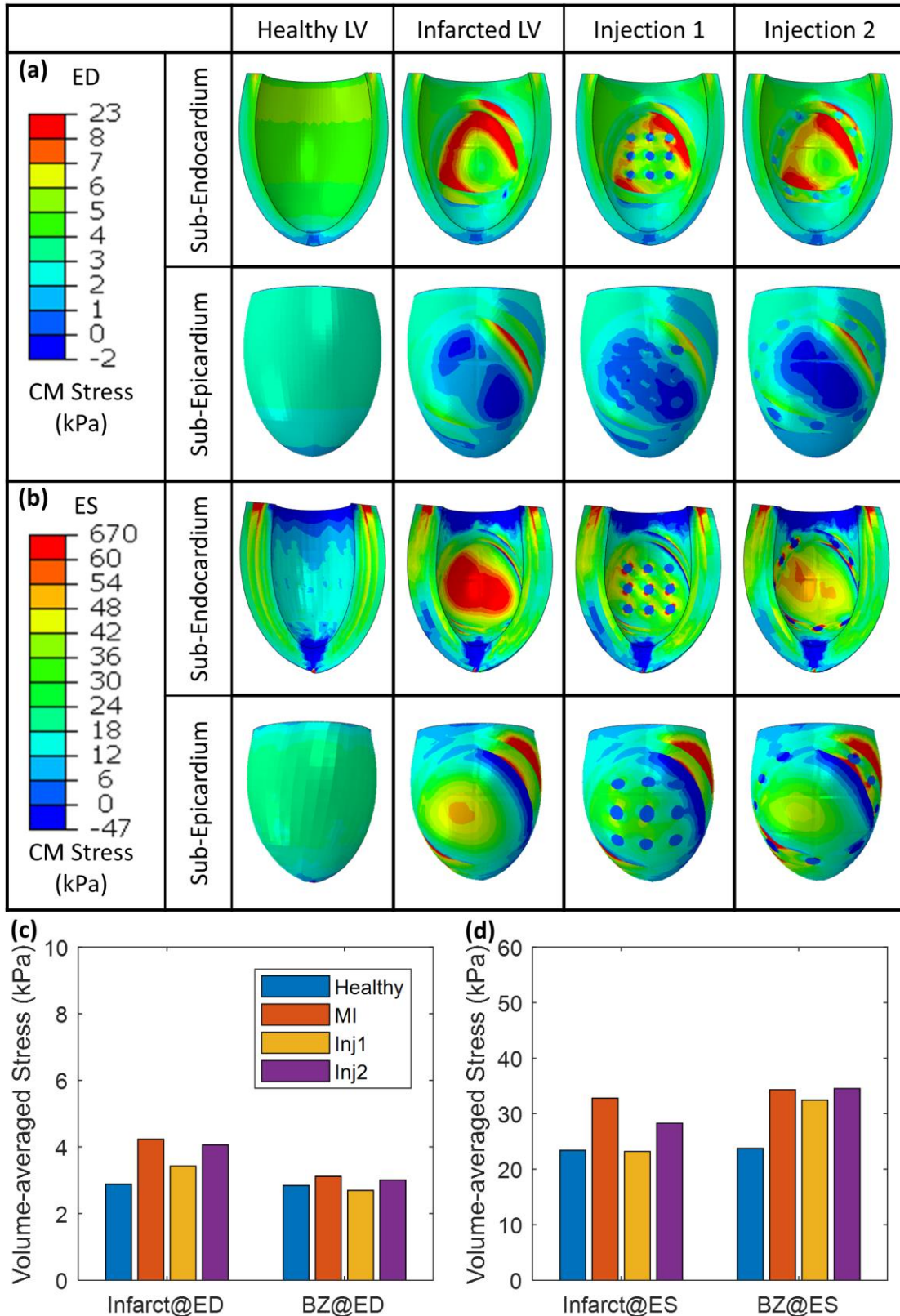


Figure 6. Simulation results of the idealized model. Cardiomyocyte stress contour plots near the endocardium and epicardium are both shown at the end-diastolic (a) and the end-systolic (b) stages. The average cardiomyocyte stresses in the infarct region and the BZ in the healthy and diseased LVs are compared at the end-diastolic (c) and end-systolic (d)

stages. MI = myocardial infarct, BZ = border zone, Inj1 = Injection strategy 1, Inj2 = Injection strategy 2.

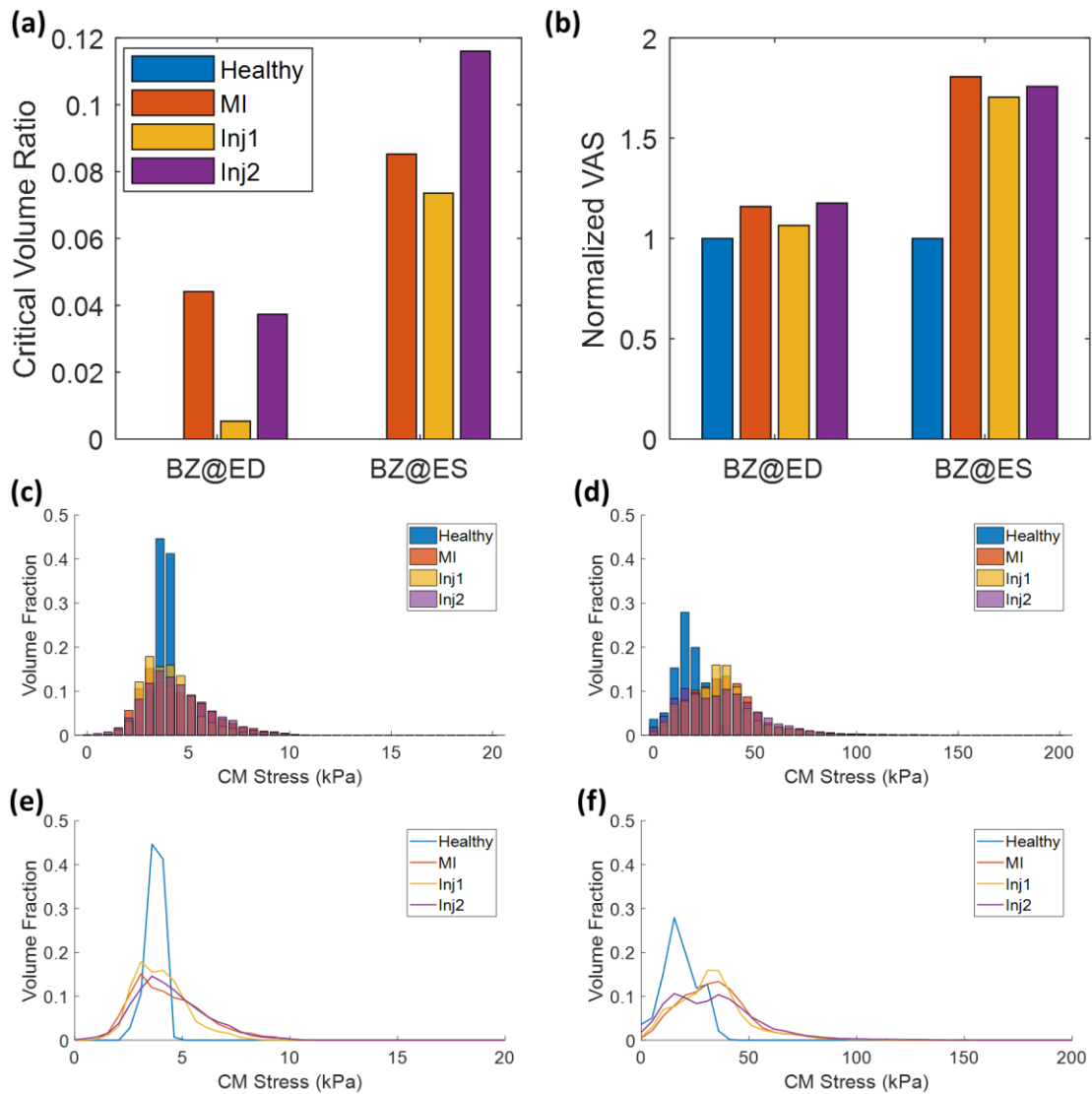


Figure 7. Cardiomyocyte stress around the endocardial border zone predicted by the Idealized model. (a) Critical volume in the endocardial BZ in each model was compared at ED and ES. (b) Volume-averaged stress (VAS) of the endocardial BZ normalized by the healthy baseline values. Endocardial stress histograms were plotted at ED (c) and ES (d). (e, f) Corresponding distribution lines to the histograms.

DTI-based Model Stresses

In the stress contour plots of the DTI-based model at ED (Fig. 8a), MI was found to induce endocardial stresses due to the reduced wall thickness and increased stiffness in the infarct region. The high stress regions were localized around the infarct border towards the base or the apex. Both injection patterns 1 and 2 attenuated the stresses in these regions. Injection pattern 1 had more pronounced effects. Epicardial stresses were mostly small or compressive so the injections did not show much effect in this region. At ES (Fig. 8b), the stress profile was

highly heterogeneous even in the healthy model. The effect of MI can still be seen in the sub-endocardium contour plots where high stresses were induced in the infarct and BZ, radiating out to the apex. The mechanical benefits of injections were also shown in this region where Injection 1 attenuated most of the stresses in the infarct while Injection 2 had superior stress reduction in the BZ.

The average cardiomyocyte stress in the infarct and BZ is compared in Fig. 8c,d. At ED, the MI caused cardiomyocyte stresses to increase by 62.3% in the infarct region and 29.9% in the BZ. With Injection 1, stress in the infarct region and the BZ was reduced by 5.6% and 7.1%, respectively. Less mechanical benefits at ED were shown in Injection 2 that cardiomyocyte stress was reduced by 2% in the infarct while increased by 5.4% in the BZ. At ES, infarct stress in the diseased models was lower than in the healthy model. However, the injection benefits were shown in the BZ where the 25.4% MI induced cardiomyocyte stress were attenuated by 9.5% and 17.4% after Injection 1 and Injection 2, respectively.

Using the same critical stress threshold values as in the Idealized case, the CSV at ED in the MI model was initially 8.9 mm³, reduced to 7.8 mm³ after Injection 2 but increased to 9.6 mm³ after Injection 1. At ES, the CSV increased to 14.0 mm³. Surprisingly, the CSV in the MI model was predicted to be smaller at 11.2 mm³, but as expected, it was further reduced after Injection 1 (9.5 mm³) and Injection 2 (8.2mm³).

Isolating the cardiomyocyte stress around the endocardial BZ (Fig. 9), the critical volume ratio was reduced by both injection methods at ES but was increased at ED. The normalized VAS plot shows a similar trend. The stress distribution histograms (Fig. 9c,d) of all diseased models showed a higher stress range than the healthy model but less difference was predicted between the MI model and two injection models. The stress histograms of other regions are shown in Fig. S2.

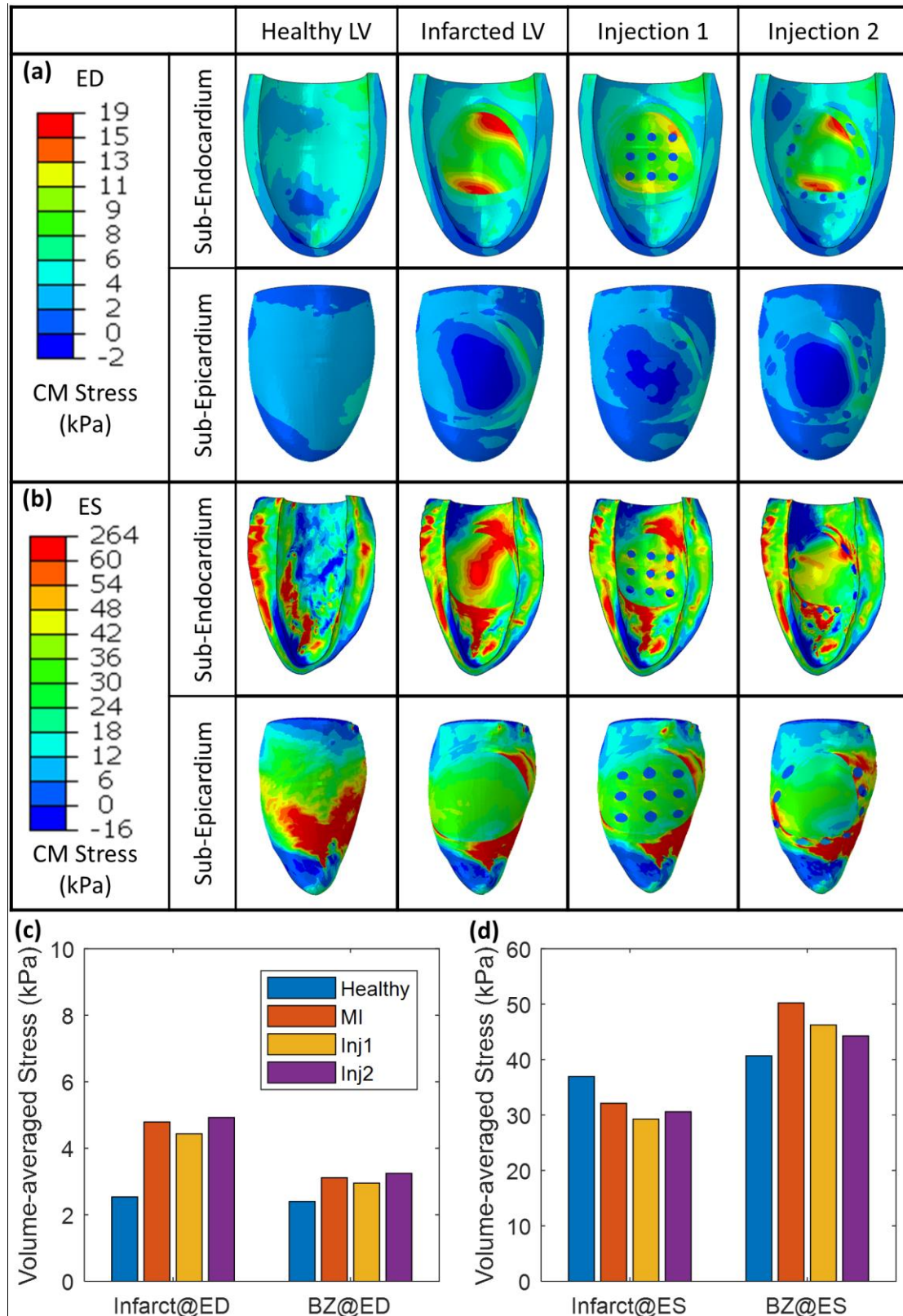


Figure 8. Simulation results of the DTI-based model. Cardiomyocyte stress contour plots near the endocardium and epicardium are both shown at the end-diastolic (a) and the end-systolic (b) stages. The average cardiomyocyte stresses in the infarct region and the BZ in

the healthy and diseased LVs are compared at the end-diastolic (c) and end-systolic (d) stages. MI = myocardial infarct, BZ = border zone, Inj1 = Injection strategy 1, Inj2 = Injection strategy 2.

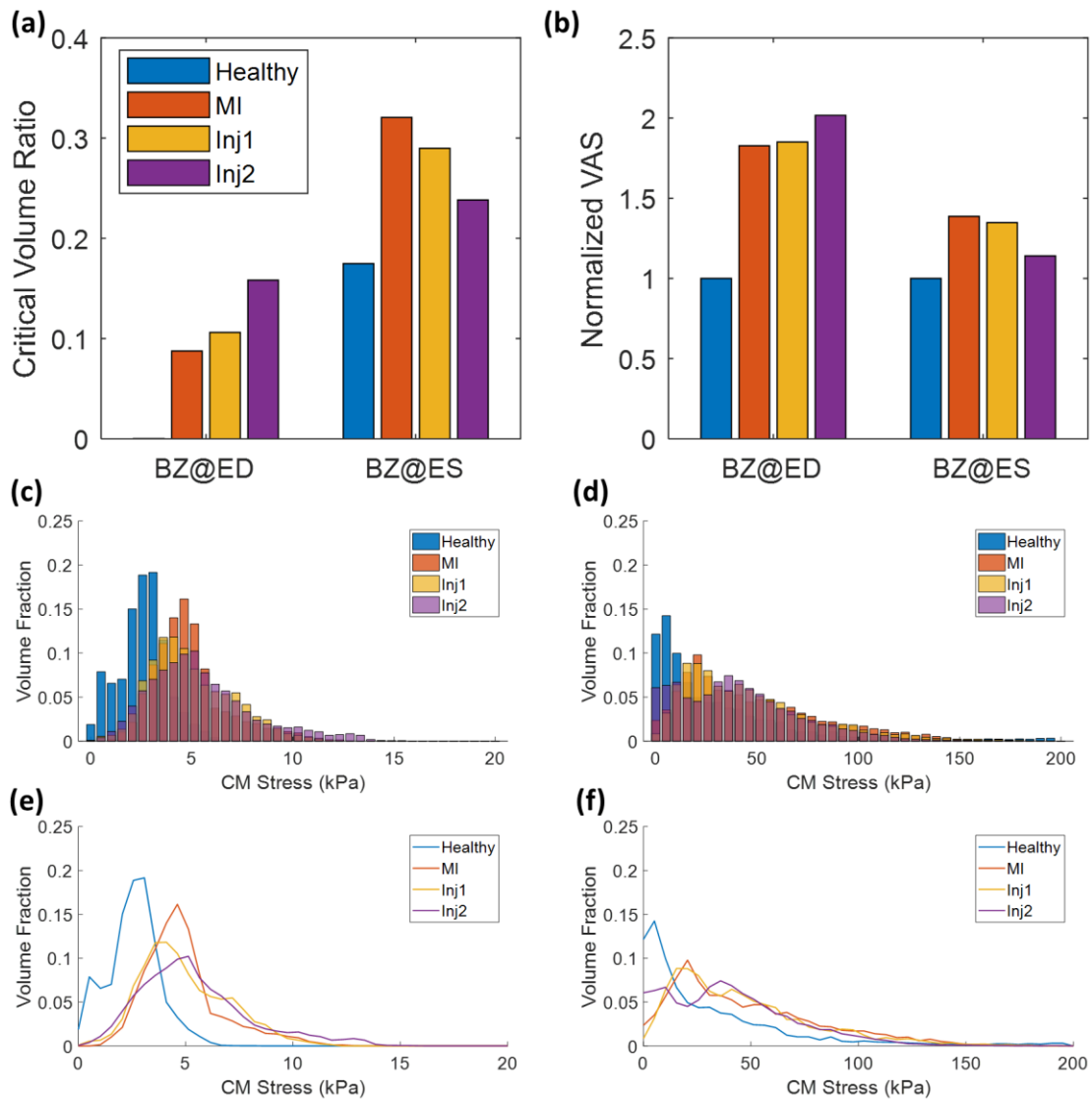


Figure 9. Cardiomyocyte stress around the endocardial border zone predicted by the DTI-based model. (a) Critical volume in endocardial BZ in each model were compared at both ED and ES. (b) Volume-averaged stress (VAS) of the endocardial BZ normalized by the healthy baseline values. Endocardial stress histograms were plotted at ED (c) and ES (d). (e, f) Corresponding distribution lines to the histograms.

Discussion

In this study, we present two quasi-static finite element simulations to model cardiac mechanics and intra-myocardial injection strategies. The models correspond to an idealized

and a DTI-based geometry and incorporate rule-based and image-based muscle cardiomyocyte orientations, respectively. Since we describe a quasi-static model of the ED and ES stages, we simplify the active myocardial model by using a thermal analogy to implement anisotropic strain. In a comparison of each model with reported baseline clinical values, both models predict clinical ranges for EF and SWT during contraction. The idealized model also captures the twisting motion of the heart, unlike the DTI-based. The current 'gold standard' to validate the model is to compare its strain prediction with *in vivo* measurement either from tagged magnetic resonance imaging [37] or from echocardiography [20]. The cardiomyocyte stresses predicted by our models are within the range of stresses predicted by validated models. Specifically, volume-averaged stress predictions in both the idealized model (2.84 kPa in ED and 23.4 kPa in ES) and the DTI model (2.53 kPa in ED and 36.08 kPa in ES) are within the ranges of stresses predicted by reported computational models (2.1 ± 4.2 kPa in ED and 23.2 ± 19.8 kPa in ES) that were validated by comparing predicted strains to echocardiographic measurements. [20].

We simulate a myocardial infarct in both models by changing the thickness and stiffness of a section of the LV wall and subsequently simulate two different injection strategies for each in the infarct and the border zone respectively. We use cardiomyocyte stresses to predict therapy efficacy. This is a reasonable indicator of efficacy as wall tension is associated with cardiomyocyte contraction, and is the primary contributor to myocardial oxygen consumption[38]. A reduction in cardiomyocyte stress can therefore reduce the overall myocardial oxygen consumption and work done by the heart tissue. Both the simple model and DTI-based model show a level of stress reduction after intra-myocardial injection.

The quantitative analyses (volume-averaged stress and critical stress volume) in the Idealized models predict that injection in the infarct (Injection 1) has a greater stress attenuation effect than injection in the BZ (Injection 2) at both ED and ES. For the DTI-based model, Injection 1 is also predicted to have better performance than Injection 2 except for in the BZ during systole. However, when the evaluation is focused on the endocardial BZ, the results are much less consistent: Injection 2 is superior to Injection 1 at ES but vice-versa at ED. Moreover, both the CSV and VAS indexes are higher after injections. This issue may result from the heterogeneity of obtained cardiomyocyte orientation which can cause aberrant stress concentrations. According to the contour plot of the healthy model, both the endocardium and epicardium contain these heterogeneous regions. Wall-thinning (MI) and wall-thickening (Inj1, Inj2) modifications might exclude or re-include some of these regions.

Both the direct infarct injection [8–10] and BZ injection[39–41] have shown functional benefits experimentally. To our knowledge, an experimental comparison of these two injection strategies has not been reported. The discrepancy of our Idealized and DTI-based model at ES could be due to the strong dependence of ES stress on active contractile force generated by cardiomyocytes. Therefore, the passive mechanical reinforcement imparted by the injections has a substantial impact on diastole but much less on systole. The ED simulations for both cases predict that the direct infarct injection strategy is superior to the

border zone injection strategy for the goal of BZ stress reduction. This is clinically important, as the BZ tissue is viable tissue, and can be salvaged by effective therapy. However, BZ injection strategies are being explored especially in regenerative therapies [39,41]. Further direct comparisons between these strategies, or combinations, are warranted in computational and experimental settings to fully elucidate the optimal injection locations for maximum clinical benefit.

The DTI-based model has higher fidelity in terms of anatomical structure compared to the simple geometry model. However, the current model has inherent limitations. The discrepancies in results may stem from the simulated mechanics as follows: sheetlet structures are known to be highly discontinuous, with V-shaped and herring-bone arrangements[28], which was not accounted for in our model. Additionally, the *ex vivo* DTI data was taken to represent ED. However, we observed that the LV elongated unnaturally in systole in the model, leading to abnormal deformation at ES. This may explain why EF values (Table S4) in the DTI-based models are lower than in the idealized models. For simulation purposes, the papillary muscles were removed to ensure the endocardial surface remained smooth for meshing and applying pressure, but this truncation causes some inherent discontinuity. The myocardium was modeled as transversely isotropic, implying that it is isotropic in the cross-cardiomyocyte plane, which is a simplification. The sheetlet and the sheetlet-normal directions were assigned the same stiffness and expansion coefficient. A recent study with cardiac DTI has shown that the myocardium is entirely anisotropic and that sheetlet shear is a dominant source of wall thickening[27]. Therefore, the myocardium constitutive model should include anisotropy in the cross-cardiomyocyte plane. To simulate wall thickening, we used global fractional shortening values, which may be higher than those reported for individual cardiomyocytes [42].

We intend to further improve our mechanical modelling enhanced in the future to incorporate anatomies and motion trajectories of increasing complexity [43,44]. For higher fidelity mapping in our future studies, conducting DT-MRI scanning on a heart *in vivo*, and subsequently conducting high-resolution DT-MRI on the same heart *ex vivo* will allow us to employ reverse finite element analysis to map end systolic cardiomyocyte orientation to *in vivo* DT-MRI data. Further, the geometries of the injections may not truly recreate wall thickening in different regions based on injection patterns. Currently, post-injection wall thickening is described in various *in vivo* studies[7–10]. These studies reported very different levels of wall thickening (ranging from 14% to 80%) which would have a major effect on stress attenuation based on the LaPlace's law. Moreover, the injections might also change the cardiomyocyte orientation of the surrounding tissue leading to a different stress distribution. Therefore, DTI data for healthy, infarcted and injected hearts should be obtained, allowing faithful reconstruction of the diseased and treated model in the future.

Although the effect of stress attenuation is shown, the increase of EF observed in various *in vivo* studies with intra-myocardial injection was not adequately simulated. The changes in EF

between healthy, MI, and treated LVs are very small and similar in the idealized and DTI-based models. Observed changes in EF are likely due to the changes of wall thickness. Our simulations did not take long-term LV remodeling into account, which is responsible for the decrease in EF between healthy and MI models. Regarding the active myocardium model, although active strain approach that we used in our study is more mathematically robust, the active stress approach is known to be more physiologically correct [21]. Future *in silico* studies will implement one of the time-dependent active stress models (for example the calcium concentration-based model [32]) so that the simulation will become dynamic. It will not only predict more accurate physiological features but will also allow for implementation of cardiac growth models to simulate the post-MI remodeling process. In addition, we only focus on rat hearts in this study. It is reported that the ventricular geometry, the fiber-like cardiomyocyte orientation, and the cardiac physiological functions are different in different species (for example rat, sheep and human)[45]. Therefore, further *in silico* studies should also take interspecies variation into consideration and simulate the intra-myocardial injection on hearts in different species.

While this study considers one model biomaterial, further work could include accurately simulating a panel of biomaterials that have been employed for intra-myocardial injection. For example, natural biomaterials such as alginate, fibrin and collagen, have high biocompatibility and accessibility and have been used previously in many early stage myocardial injection experiments[9,10,46,47]. Synthetic biomaterials, although more likely to cause inflammatory and foreign body reactions, have controllable mechanical properties such as stiffness, degradability and diffusivity, and thus have been used in recent studies to gain insights into the mechanisms of action of this therapy[8,14,48–50]. Researchers have also varied parameters such as post-MI injection timing[9] and duration of clinical benefit[8,50], and optimization of these parameters may benefit from clinically relevant models. Future studies will incorporate more accurate injection material models for different types of biomaterial and a direct comparison with an *in vivo* study to fully validate the simulation framework.

Overall, we have developed a framework to simulate the mechanical effects of intra-myocardial injection combined with DTI-based geometry and realistic fiber-like cardiomyocyte orientation. Both the simple and DTI-based models demonstrate that biomaterial injection can reduce MI-induced stresses. The four main contributions of this work can be distilled as follows;

- We have developed idealized and DTI-based finite element left-ventricular models that can capture reported cardiac functional parameters for both healthy and diseased hearts.
- The idealized model, while is less anatomically accurate than the DTI-based model, is less computationally-intensive and can capture reported experimental ranges for clinical parameters, such as LV twist more realistically.
- Both models show that intra-myocardial injections can reduce cardiomyocyte stress after MI.
- According to the Idealized model, injections into the infarct are predicted to be superior

in reducing border zone cardiomyocyte stress than injections in the BZ. However, the BZ injections are predicted to attenuate stress at ES in the DTI model. Additional subject-specific models with carefully controlled injection patterns should be simulated in future works to confirm this.

In summary, a computational LV model may be employed as a tool for guiding optimal intra-myocardial injection strategies and biomaterial properties. Furthermore, this model has potential to aid fundamental understanding and reveal insights into intra-myocardial injection therapy, and to aid with its clinical translation for the prevention or treatment of post-MI heart failure.

Acknowledgements

The authors would like to thank Ronghli Liao PhD, Sudeshna Fisch PhD and Souen Ngoy from the Brigham and Women's Hospital (BWH) Rodent Cardiovascular Physiology core for their technical support for animal studies, Eimear Dolan PhD from NUI Galway for providing the HA-PH-RGD hydrogel properties, and the Irish Centre for High-End Computing (ICHEC) for computational studies. YF acknowledges a Summer scholarship from NUI Galway.

References

1. World Health Organization. Top 10 causes of death worldwide. Fact Sheet 2017. <http://www.who.int/mediacentre/factsheets/fs310/en/>. Accessed March 5, 2017.
2. Holmes JW, Borg TK, Covell JW. Structure and Mechanics of Healing Myocardial Infarcts. *Annual Review of Biomedical Engineering* 2005; **7**(1):223–253. doi:10.1146/annurev.bioeng.7.060804.100453.
3. Simon MA, Watson J, Baldwin JT, Wagner WR, Borovetz HS. Current and Future Considerations in the Use of Mechanical Circulatory Support Devices. *Annual Review of Biomedical Engineering* 2008; **10**(1):59–84. doi:10.1146/annurev.bioeng.9.060906.151856.
4. Roche ET, Horvath MA, Wamala I, et al. Soft robotic sleeve supports heart function. *Science Translational Medicine* 2017; **9**(373). doi:10.1126/scitranslmed.aaf3925.
5. O’Neill HS, Gallagher LB, O’Sullivan J, et al. Biomaterial-Enhanced Cell and Drug Delivery: Lessons Learned in the Cardiac Field and Future Perspectives. *Advanced Materials* 2016:5648–5661.
6. Ota T, Patronik NA, Schwartzman D, Riviere CN, Zenati MA. Minimally invasive epicardial injections using a novel semiautonomous robotic device. *Circulation* 2008; **118**(14 Suppl). doi:10.1161/CIRCULATIONAHA.107.756049.
7. Nelson DM, Ma Z, Fujimoto KL, Hashizume R, Wagner WR. Intra-myocardial biomaterial injection therapy in the treatment of heart failure: Materials, outcomes and challenges. *Acta biomaterialia* 2011; **7**(1):1–15. doi:10.1016/j.actbio.2010.06.039.
8. Dobner S, Bezuidenhout D, Govender P, Zilla P, Davies N. A Synthetic Non-degradable Polyethylene Glycol Hydrogel Retards Adverse Post-infarct Left Ventricular Remodeling. *Journal of Cardiac Failure* 2009; **15**(7):629–636. doi:10.1016/j.cardfail.2009.03.003.
9. Landa N, Miller L, Feinberg MS, et al. Effect of Injectable Alginate Implant on Cardiac Remodeling and Function After Recent and Old Infarcts in Rat. *Circulation* 2008; **117**(11):1388–1396. doi:10.1161/CIRCULATIONAHA.107.727420.
10. Dai W, Wold LE, Dow JS, Kloner RA. Thickening of the Infarcted Wall by Collagen Injection Improves Left Ventricular Function in Rats. *Journal of the American College of Cardiology* 2005; **46**(4):714–719. doi:10.1016/j.jacc.2005.04.056.
11. Göktepe S, Acharya SNS, Wong J, Kuhl E. Computational modeling of passive myocardium. *International Journal for Numerical Methods in Biomedical Engineering* 2011; **27**(1):1–12. doi:10.1002/cnm.1402.
12. Kichula ET, Wang H, Dorsey SM, et al. Experimental and Computational Investigation of Altered Mechanical Properties in Myocardium after Hydrogel Injection. *Annals of Biomedical Engineering* 2014; **42**(7):1546–1556. doi:10.1007/s10439-013-0937-9.
13. Wall ST, Walker JC, Healy KE, Ratcliffe MB, Guccione JM. Theoretical Impact of the Injection of Material Into the Myocardium. *Circulation* 2006; **114**(24).
14. Rodell CB, Lee ME, Wang H, et al. Injectable Shear-Thinning Hydrogels for Minimally Invasive Delivery to Infarcted Myocardium to Limit Left Ventricular Remodeling. *Circulation: Cardiovascular Interventions* 2016; **9**(10):1–11. doi:10.1161/CIRCINTERVENTIONS.116.004058.

15. Fung YC, Fronek K, Patitucci P. Pseudoelasticity of arteries and the choice of its mathematical expression. *The American journal of physiology* 1979; **237**(5):H620–H631.
16. Wenk JF, Eslami P, Zhang Z, et al. A novel method for quantifying the in-vivo mechanical effect of material injected into a myocardial infarction. *Annals of Thoracic Surgery* 2011; **92**(3):935–941. doi:10.1016/j.athoracsur.2011.04.089.
17. Holzapfel GA, Ogden RW. Constitutive modelling of passive myocardium: a structurally based framework for material characterization. *Phil. Trans. R. Soc. A* 2009; **367**:3445–3475. doi:10.1098/rsta.2009.0091.
18. Genet M, Lee LC, Kuhl E, Guccione J. Abaqus / Standard - based quantification of human cardiac mechanical properties. *SIMULIA Community Conference* 2014:1–14.
19. Baillargeon B, Rebelo N, Fox DD, Taylor RL, Kuhl E. The Living Heart Project: A robust and integrative simulator for human heart function. *European journal of mechanics. A, Solids* 2014; **48**:38–47. doi:10.1016/j.euromechsol.2014.04.001.
20. Sack KL, Aliotta E, Ennis DB, et al. Construction and Validation of Subject-Specific Biventricular Finite-Element Models of Healthy and Failing Swine Hearts From High-Resolution DT-MRI. *Frontiers in Physiology* 2018; **9**:539. doi:10.3389/fphys.2018.00539.
21. Ambrosi D, Pezzuto S. Active Stress vs. Active Strain in Mechanobiology: Constitutive Issues. *J Elast* 2012; **107**:199–212. doi:10.1007/s10659-011-9351-4.
22. Ambrosi D, Arioli G, Nobile F, Quarteroni A. ELECTROMECHANICAL COUPLING IN CARDIAC DYNAMICS: THE ACTIVE STRAIN APPROACH *. *SIAM J. APPL. MATH* **71**(2):605–621. doi:10.1137/100788379.
23. Nardinocchi P, Teresi L. On the Active Response of Soft Living Tissues. 2007; **88**:27–39. doi:10.1007/s10659-007-9111-7.
24. Balaban G, Finsberg H, Odland HH, et al. High-resolution data assimilation of cardiac mechanics applied to a dyssynchronous ventricle. *International Journal for Numerical Methods in Biomedical Engineering* 2017; **33**(11):e2863. doi:10.1002/cnm.2863.
25. Wenk JF, Wall ST, Peterson RC, et al. A Method for Automatically Optimizing Medical Devices for Treating Heart Failure: Designing Polymeric Injection Patterns. *Journal of Biomechanical Engineering* 2009; **131**(12):121011. doi:10.1115/1.4000165.
26. Kortsmits J, Davies NH, Miller R, Macadangdang JR, Zilla P, Franz T. The effect of hydrogel injection on cardiac function and myocardial mechanics in a computational post-infarction model. *Computer Methods in Biomechanics and Biomedical Engineering* 2013; **16**(11):1185–1195. doi:10.1080/10255842.2012.656611.
27. Nielles-Vallespin S, Khalique Z, Ferreira PF, et al. Assessment of Myocardial Microstructural Dynamics by In Vivo Diffusion Tensor Cardiac Magnetic Resonance. *Journal of the American College of Cardiology* 2017; **69**(6):661–676. doi:10.1016/j.jacc.2016.11.051.
28. Teh I, McClymont D, Burton RAB, et al. Resolving Fine Cardiac Structures in Rats with High-Resolution Diffusion Tensor Imaging. *Scientific Reports* 2016; **6**(1):30573. doi:10.1038/srep30573.
29. Dassault Systèmes. ABAQUS 2018 Documentation. 2018.
30. Quinn KP, Sullivan KE, Liu Z, et al. Optical metrics of the extracellular matrix predict

- compositional and mechanical changes after myocardial infarction. *Scientific Reports* 2016; **6**(1):35823. doi:10.1038/srep35823.
31. Torrent-Guasp F, Ballester M, Buckberg GD, et al. Spatial orientation of the ventricular muscle band: Physiologic contribution and surgical implications. *The Journal of Thoracic and Cardiovascular Surgery* 2001; **122**(2):389–392. doi:10.1067/mtc.2001.113745.
 32. Guccione JM, McCulloch AD. Mechanics of active contraction in cardiac muscle: Part I- Constitutive relations for fiber stress that describe deactivation. *Journal of biomechanical engineering* 1993; **115**(1):72–81. doi:10.1115/1.2895473.
 33. Watson LE, Sheth M, Denyer RF, Dostal DE. Baseline Echocardiographic Values for Adult Male Rats. *Journal of the American Society of Echocardiography* 2004; **17**(2):161–167. doi:10.1016/j.echo.2003.10.010.
 34. Dolan EB, Kovarova L, O’Neill H, et al. A dvanced M aterial Cath eter (AMCath), a minimally invasive endocardial catheter for the delivery of fast-gelling covalently cross-linked hyaluronic acid hydrogels. *Journal of Biomaterials Applications* 2018; **33**(5):681–692. doi:10.1177/0885328218805878.
 35. McEvoy E, Holzapfel GA, McGarry P. Compressibility and Anisotropy of the Ventricular Myocardium: Experimental Analysis and Microstructural Modeling. *Journal of Biomechanical Engineering* 2018; **140**(8):081004. doi:10.1115/1.4039947.
 36. Nagel E, Stuber M, Burkhard B, et al. Cardiac rotation and relaxation in patients with aortic valve stenosis. *European Heart Journal* 2000; **21**(7):582–589. doi:10.1053/euhj.1999.1736.
 37. Genet M, Chuan Lee L, Nguyen R, et al. Distribution of normal human left ventricular myofiber stress at end diastole and end systole: a target for in silico design of heart failure treatments. *J Appl Physiol* 2014; **117**:142–152. doi:10.1152/jappphysiol.00255.2014.-Ven.
 38. Baller D, Wolpers HG, Hoeft A, et al. Increase of myocardial oxygen consumption due to active diastolic wall tension. *Basic research in cardiology* **79**(2):176–85. <http://www.ncbi.nlm.nih.gov/pubmed/6146304> Accessed January 16, 2018.
 39. Hsieh PCH, Davis ME, Gannon J, MacGillivray C, Lee RT. Controlled delivery of PDGF-BB for myocardial protection using injectable self-assembling peptide nanofibers. *The Journal of clinical investigation* 2006; **116**(1):237–48. doi:10.1172/JCI25878.
 40. Suarez SL, Rane AA, Muñoz A, et al. Intramyocardial injection of hydrogel with high interstitial spread does not impact action potential propagation. *Acta biomaterialia* 2015; **26**:13–22. doi:10.1016/j.actbio.2015.08.004.
 41. Bastings MMC, Koudstaal S, Kieltyka RE, et al. A Fast pH-Switchable and Self-Healing Supramolecular Hydrogel Carrier for Guided, Local Catheter Injection in the Infarcted Myocardium. *Advanced Healthcare Materials* 2014; **3**(1):70–78. doi:10.1002/adhm.201300076.
 42. Axel L, Wedeen VJ, Ennis DB. Probing dynamic myocardial microstructure with cardiac magnetic resonance diffusion tensor imaging. *Journal of cardiovascular magnetic resonance : official journal of the Society for Cardiovascular Magnetic Resonance* 2014; **16**(1):89. doi:10.1186/s12968-014-0089-6.

43. Hales PW, Schneider JE, Burton RAB, Wright BJ, Bollensdorff C, Kohl P. Histo-anatomical structure of the living isolated rat heart in two contraction states assessed by diffusion tensor MRI. *Progress in Biophysics and Molecular Biology* 2012; **110**(2–3):319–330. doi:10.1016/j.pbiomolbio.2012.07.014.
44. Lohezic M, Teh I, Bollensdorff C, et al. Interrogation of living myocardium in multiple static deformation states with diffusion tensor and diffusion spectrum imaging. *Progress in Biophysics and Molecular Biology* 2014; **115**(2–3):213–225. doi:10.1016/j.pbiomolbio.2014.08.002.
45. Mekkaoui C, Huang S, Chen HH, et al. Fiber architecture in remodeled myocardium revealed with a quantitative diffusion CMR tractography framework and histological validation. *Journal of Cardiovascular Magnetic Resonance* 2012; **14**(1). doi:10.1186/1532-429X-14-70.
46. Christman KL, Fok HH, Sievers RE, Fang Q, Lee RJ. Fibrin Glue Alone and Skeletal Myoblasts in a Fibrin Scaffold Preserve Cardiac Function after Myocardial Infarction. *Tissue Engineering* 2004; **10**(3–4):403–409. doi:10.1089/107632704323061762.
47. Mukherjee R, Zavadzkas JA, Saunders SM, et al. Targeted myocardial microinjections of a biocomposite material reduces infarct expansion in pigs. *The Annals of thoracic surgery* 2008; **86**(4):1268–76. doi:10.1016/j.athoracsur.2008.04.107.
48. Rane AA, Chuang JS, Shah A, et al. Increased Infarct Wall Thickness by a Bio-Inert Material Is Insufficient to Prevent Negative Left Ventricular Remodeling after Myocardial Infarction. Chin W-C, ed. *PLoS ONE* 2011; **6**(6):e21571. doi:10.1371/journal.pone.0021571.
49. Hsieh PCH, MacGillivray C, Gannon J, Cruz FU, Lee RT. Local Controlled Intramyocardial Delivery of Platelet-Derived Growth Factor Improves Postinfarction Ventricular Function Without Pulmonary Toxicity. *Circulation* 2006; **114**(7):637–644. doi:10.1161/CIRCULATIONAHA.106.639831.
50. Jiang X-J, Wang T, Li X-Y, et al. Injection of a novel synthetic hydrogel preserves left ventricle function after myocardial infarction. *Journal of Biomedical Materials Research Part A* 2009; **90A**(2):472–477. doi:10.1002/jbm.a.32118.

Table 1. A summary of all left ventricle models, the infarct wall thickness, their stiffness value, relative contractility and injection location.

		Geometry	Infarct Wall thickness	Stiffness C_0 (kPa)	Contractility α_{ff}	Site of Injections
Idealized Model	Healthy	Truncated Ellipsoid	N/A	0.679	100%	N/A
	MI		50%	Infarct – 33.75	BZ – 50% Infarct – 0%	N/A
	Injection 1		80%	Infarct – 33.75	BZ – 50% Infarct – 0% Injection – 0%	Infarct
	Injection 2		60%			BZ
DTI-based Model	Healthy	Healthy Rat Heart from MRI	N/A	0.679	100%	N/A
	MI		50%	Infarct – 33.75	BZ – 50% Infarct – 0%	N/A
	Injection 1		80%	Infarct – 33.75	BZ – 50% Infarct – 0% Injection – 0%	Infarct
	Injection 2		60%			BZ